Estimation of a Drill Hole's Center Location from the Wavefront in Scattering Waves Visualized by Pulsed Laser Scanning

Tetsuya Yamamoto[*1], Hiroshi Tsuda[1], Junji Takatsubo[2]

[1]Research Institute of Instrumentation Frontier (RIIF), National Institute of Advanced Industrial Science and Technology (AIST), AIST Tsukuba Central 2, Tsukuba, Ibaraki 305-8568, Japan

[2]Tsukuba Technology Co., Ltd. 2-1-6-214, Sengen, Tsukuba, Ibaraki 305-0047, Japan

[*1]tetsuya.yamamoto@aist.go.jp

Abstract- **The center location of a defect (a drill hole, DH) in a solid material was estimated using the circular-shaped wavefront of scattering waves. Measurement data recorded by a pulsed laser scanning system were used in the calculation. For data preprocessing, two techniques were applied: with the waveform peaks being extracted from the original measurement signals, and then a suitable threshold level being applied to the peak-extracted data. The center location of the hole was detected using the scattering wavefront of the snapshot images obtained immediately after reflection from the hole. Efficient calculation can be achieved as a result of decreasing a great number of pixel points in the snapshot images. This imaging technique is a promising candidate for use in an automatic defect inspection system that employs ultrasonic waves excited by pulsed laser scanning.**

Keywords- Defect Detection; Pulsed Laser Scanning; Scattering Wave; Non-Destructive Inspection; Drill Hole

I. INTRODUCTION

The time-varying scattering behavior of ultrasonic waves propagating through solid materials can contribute greatly to the detection of defects in the material by non-destructive inspectors and non-experts alike. This visualization technique is a major technological breakthrough compared to the conventional pulsed-echo method, in which defects, flaws, and cracks must be detected using amplitude and phase waveforms (echo signals). Echo signals are complex and intricate waveforms that include reflected, diffracted, and mode-converted waves. Even when echo signals are being interpreted by non-destructive experts, the echo signals from the defects sometimes lead to misunderstandings and overestimation.

We developed an imaging system using ultrasonic-wave propagation [1–8]. In this system, ultrasonic waves that are thermoelastically generated by a scanning pulsed laser propagate through the solid material, and are then received at a transducer attached on the surface of the specimen. Under the assumption of the reciprocity principle of wave propagation [4], the wave propagation can be visualized as if the waves are generated from the transducer and propagated through the material. Compared to the conventional method that uses a laser vibrometer as a receiving probe [9], this system has an advantage in that the laser irradiation can be treated independently of the incident angle and focal length. Therefore, this system makes it possible to visualize the ultrasonic-wave propagation behaviors even in complex-shaped structures such as helical-shaped drill blades, elbow pipes with artificial corrosion of the inner surface, delamination of carbon fiber-reinforced plastics (CFRPs), composite skin-stringer structures, and steel plates with butt welding [5–7]. Moreover, the optimum measurement conditions of the laser for various types of specimens, such as scanning frequency, scanning pitch, beam diameter, incident angle, and irradiation distance, have also been examined and investigated [5–7]. As a next step in this work, we believe it would be desirable for any user, even non-experts, to automatically obtain the key features of the defect, such as the location and the size, just by setting simple measurement conditions.

In computer vision and image processing, face detection is a hot research topic. Viola and Jones proposed a progressive method for face detection which is now widely used and has become one of the standard techniques because of its robustness, high detection accuracy, and rapid computational time [10, 11]. Digital cameras now come equipped with this image processing technique that can not only identify a face but also provide real-time tracking of the face in accord with its movement. A technique based on the Viola-Jones method is also used in security camera systems. In visual nondestructive testing using ultrasonic waves, however, the development of an original image processing technique is indispensable. The shape of the scattering waves that depend upon the properties of the crack or flaw is not necessarily pre-defined as is a human face. Unlike face detection using Viola-Jones method, therefore, a great number of image samples for prior learning cannot be prepared in the case of nondestructive inspection. Moreover, the intensity of the scattering waves obtained by the inspection equipment is weak and the scattering waves are often hidden behind the incident waves with larger amplitude, that is, the image is not as sharp as the face image in a photograph in which the person is assumed to be standing in front of the camera. In addition, the received waveforms consist of not only transmitted waves from the transducer and reflected waves from the defects and specimen periphery but also mode-converted waves; thus, the image processing of visual nondestructive inspection is extremely troublesome. As noted above, a conventional image detection technique such as that used for face detection cannot be applied to a visual defect detection system for nondestructive inspection using ultrasonic waves.

Several visual nondestructive inspection techniques using ultrasonic waves have been attempted and reported. For example, as a visual nondestructive inspection technique, photoelasticity is a well-known imaging method, and wave propagation behaviors observed with photoelasticity have been reported [12–14]. However, this method can be applied only to transparent materials. Scales and Malcolm reported the visualization of ultrasonic wave propagation [15]. They mainly discussed the wave propagation mechanism in random media, and they used lasers for both the excitation and detection of ultrasonic waves; their measurement setups are also different from ours. Michaels et al. measured ultrasonic waves and visualized outward traveling waves from a source, reflected waves from specimen boundaries, and scattering waves from discontinuities [16, 17]. They used two transducers: a source transducer mounted on the back surface of the specimen, and an air-coupled transducer scanned to acquire the data. Because they used an air-coupled probe, the scattered signal was weak and it was thus necessary to remove the source wave to highlight the scattered waves, in a rather laborious procedure. Moreover, because of the restrictions for the angle and the distance for the specimen required by the air-coupled probe, a specimen is restricted to a simple shape such as a plate, and this means that only the Lamb waves propagating through the plate are measured. In these prior reports of visual inspection, the key features of the defect such as the location and the size were not discussed.

In the present study, by focusing on the circular-shaped wavefront of the scattering waves from a defect, we estimated the center location of the defect. A specimen with a drill hole (DH) as the defect at the center of an aluminum alloy plate was used throughout the study. Measurement data recorded by scanning the pulsed laser irradiation are used for the estimation. Two data preprocessing steps are used: the waveform peaks are extracted from the original measurement signals, and then a threshold level is applied to the peak-extracted data. The defect location is then estimated by using the preprocessed pixel points in the snapshot images. The center location of the hole is detected in the snapshot images obtained immediately after reflection from the defect. Efficient estimation can be obtained by reducing the number of pixel points; that is, the workload is decreased due to the reduction in non-zero points used in estimating the defect center location. Although defect detection using laser-excited ultrasonic-wave movies makes it easy even for non-experts to identify the presence of a structural defect, it is still difficult to pinpoint the exact defect location. The visual defect detection technique proposed in the present study is a promising candidate for use with automatic defect detection systems.

II. EXPERIMENTAL PROCEDURE

Figure 1 shows the ultrasonic wave inspection system using pulsed laser scanning. When the surface of a specimen is subjected to transient heating by pulsed laser irradiation, ultrasonic waves are produced as a result of surface motion that is due to thermal expansion. The transient displacement by thermal expansion on the material surface, generated by pulsed laser irradiation, is detected by a transducer (AET FC500; 19 mm element dia., 2.25 MHz nominal resonance) attached on the side wall of the specimen. The received signals are recorded in a PC in binary format with signed 8-bit integer-type via a low-noise preamplifier and a high-speed digitizer (A/D converter). Using the reciprocity principle in wave propagation, a series of successive images is produced as an animation of the wave propagation, so that ultrasonic waves are transmitted from the transducer and then propagated through the solid material.

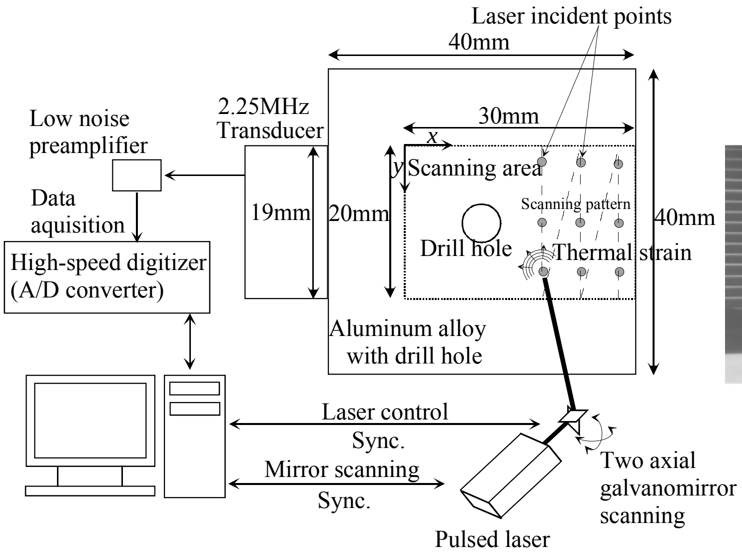

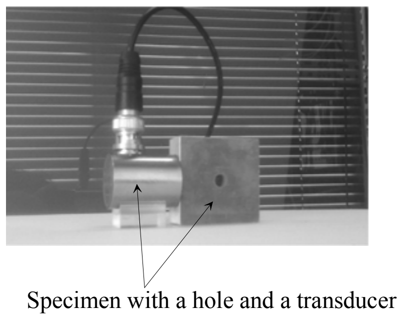

Fig. 1 The ultrasonic wave inspection system using pulsed laser scanning

Fig. 2 Photograph of a specimen with a drill hole (DH) and a transducer

Figure 2 is a photograph of the specimen with a DH and a transducer. Aluminum alloy was used as the specimen. Its dimensions were 40 mm long, 40 mm wide, and 15 mm thick with a cylindrical hole (5.6 mm dia.) at its center. The laser was scanned with 120 × 80 points (total 9600 points) in an *x*–*y* plane of 30 mm × 20 mm, so that the hole is encountered. The distance of the grid division was d*x* = d*y* = 0.25 mm, and a total of 501 timesteps (d*t* = 0.04 μs) were recorded at each grid (pixel) point in the two-dimensional plane.

Figure 3 shows the relation between the scanning area, laser incident points, and slicing plane for the scattering-wave movie. The measurement data are composed of two spatial arrays (*x* and *y*) and one time axis; that is, the data represent three-dimensional data. If two-dimensional spatial arrays in the *x*–*y* plane at a certain time *t* are extracted, the slicing plane indicates the two-dimensional snapshot of surface transient displacement distributions for the scattering-wave movie. If one spatial (*x*-axis or *y*-axis) array and the time axis *t* are extracted, the slicing plane denotes a B-scope image whose gradient presents the propagation velocity of the ultrasonic waves. It is most effective and desirable to treat the data in the way in which the wave propagation behavior can be observed in detail.

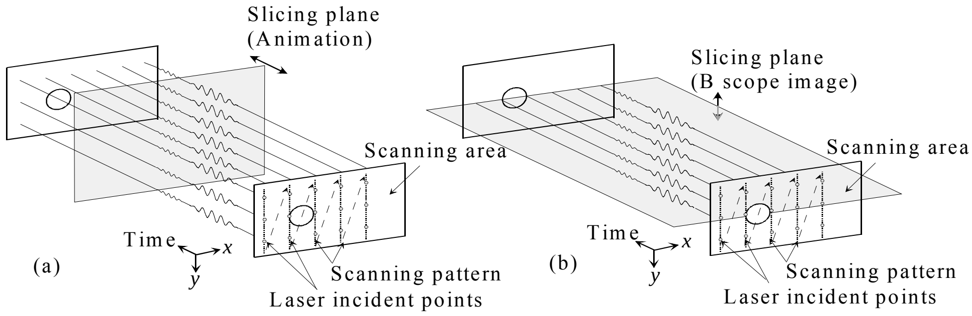

Fig. 3 Scanning area, laser incident points, and slicing plane for animation

A. Data Preprocessing

The movie of the scattering waves is created and displayed using the sequentially recorded t = 501 frames with spatial arrays of 120 × 80 points (for a total of 9600 points in the spatial plane). The measurement data, recorded using the pulsed laser scanning technique, is composed of three-dimensional arrays; each grid (pixel) point, allocated in two-dimensional space, has a time-series signal so that a series of successive images is produced as an animation of wave propagation. In the preprocessing, it is effective and desirable to treat the measurement data by taking advantage of the features of the data structure. The peaks of the data series recorded on the time axis were first extracted so that the following condition is satisfied: $(|a_{t-2}(x,y)| \le |a_{t-1}(x,y)| \le |a_t(x,y)| \ge |a_{t+1}(x,y)| \ge |a_{t+2}(x,y)|$, where $a_t(x,y)$ is the echo signal located in (*x*, *y*) at *t* timestep; only the absolute values greater than or equal to the previous and future amplitudes within two timesteps were extracted, and the remaining values were set to zero. In this case, all data are represented as either zero or non-zero (binary signal processing).

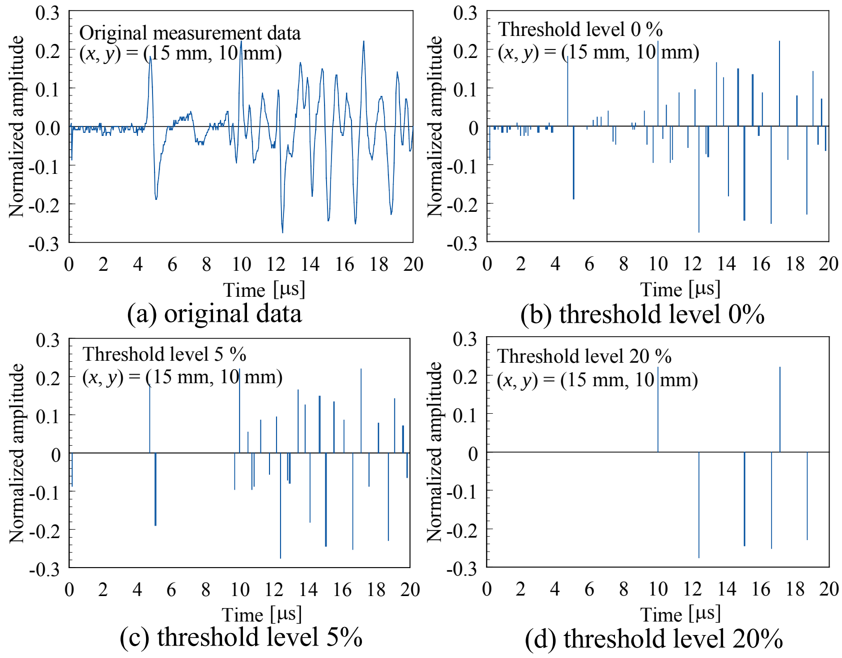

Fig. 4 Normalized amplitude as a function of time at x = 15 mm and y = 10 mm in (a) original data, (b) threshold level of 0%, (c) threshold level of 5%, (d) threshold level of 20%

Figure 4a shows the original measurement data allocated in (x, y) = (15 mm, 10 mm). The signals were normalized by the maximum amplitude value obtained at the point (x, y) = (6. 25 mm, 8.75 mm) and t = 3.64 μs (91 timesteps). As shown in Figure 4a, the waveform is complex and intricate because it includes the incident, reflected, diffracted, and mode-converted waves. Figure 4b shows the results of the peak extraction discussed above. Compared to the original measurement data (Fig. 4a), the maximum values of the peaks and the minimum values of the depressions, which are expressed by bars in the bar graph, are properly extracted. Although binary signal processing is usually demonstrated by only two fixed-amplitude values, for instance 0 and 1, the peak levels are maintained intact in this figure to observe the original features of the wave behavior. In Figure 4b, unwanted peaks with small amplitudes, especially between 0 μs and 10 μs, were observed. To enhance the accuracy of the defect detection and reduce the computational time, it is desirable to remove these weak and meaningless peaks. To do this, a threshold level is applied to the peak-extracted data. In general, if a lower threshold level is used, a great number of peaks including interfering peaks make the calculation more time-consuming and give unsatisfactory defect detection. If a higher threshold level is used, however, a small number of peaks can decrease the simulation time, but the defect is not properly detected because of insufficient information. In this study, several threshold levels were used in an attempt to determine the suitable level. The threshold level is defined as the percentage for the value obtained at (x, y) = (6.25 mm, 8.75 mm) for t = 3.64 μs, which is the signal with the maximum amplitude.

Figures 4c and d show the results for the threshold levels of 5% and 20%, respectively. As shown in Figure 4c, by setting the threshold level at 5%, the weak and unwanted peaks are clearly removed. For the threshold level of 20%, however, peaks are excessively removed, including the important ones (Fig. 4d).

1) Two-dimensional Snapshots of Surface Transient Displacement:

Figures 5Aa–d show the two-dimensional snapshots of surface transient displacement obtained by the ultrasonic wave inspection system using pulsed laser scanning. The snapshots at t = 2.8 μs, 4.2 μs, 5.6 μs, and 7.0 μs are presented. At t = 2.8 μs, the compression wave from the left side was observed as an incident wave. At t = 4.2 μs, the incident wave is reflected at the hole of the specimen (backscattered wave). At the same time, at the leftmost side, the propagation of the surface wave (shear wave) was observed. At t = 5.6 μs, the forward diffracted wave and the backscattered wave were observed. The surface wave (shear wave) was propagated further forward and reached the hole at t = 7.0 μs. Although the one-dimensional signal in Figure 4a looks very complex and it would be difficult for non-experts to correctly distinguish the reflected waves from the defect, the wave propagation mechanism can be easily grasped using the animated two-dimensional successive images.

Figures 5Ba–d show the two-dimensional snapshots using monochromatic brightness as a result of the peak extraction from the one-dimensional time-domain waveform. The timesteps are the same as in Figures 5A and B. As are shown in these figures, a similar phenomenon in wave scattering can be confirmed even after the peak extraction processing. In Figure 5B, however, unimportant peaks with small amplitudes are observed all over the laser scanning area because of the threshold level of 0%.

We applied threshold levels of 5%, 10%, and 20% to the peak-extracted data, and the results are shown in Figures 5C–E, respectively. In Figures 5Ca–d, the unwanted peaks were eliminated by applying the 5% threshold level as we did for the set-up the results of which are shown in Figure 4c. In Figures 5Da–d, the unwanted peaks were also eliminated by applying the 10% threshold level. In Figures 5Ea–d, however, the peaks were excessively removed by the increased threshold level, including part of the scattering wavefront required for estimating the defect location.

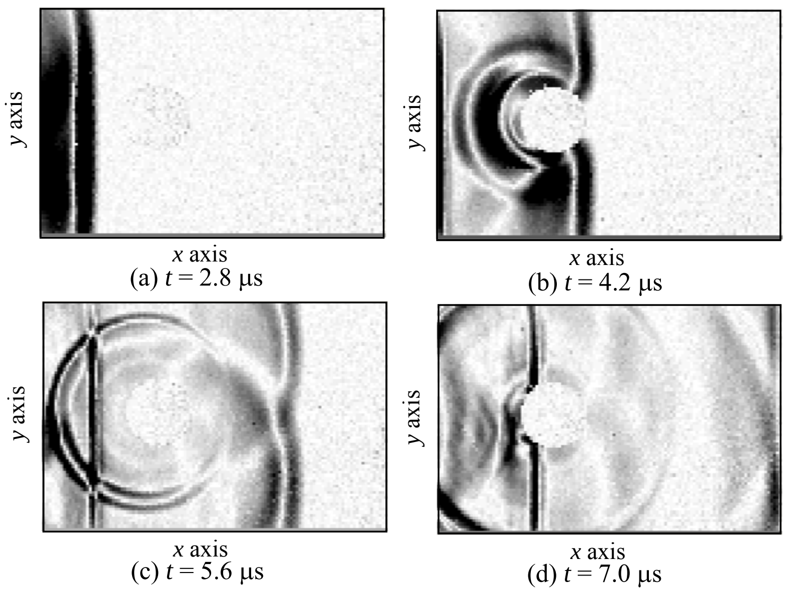

Fig. 5A Two-dimensional snapshots at (a) t = 2.8 μs, (b) t = 4.2 μs, (c) t = 5.6 μs, (d) t = 7.0 μs (original measurement data)

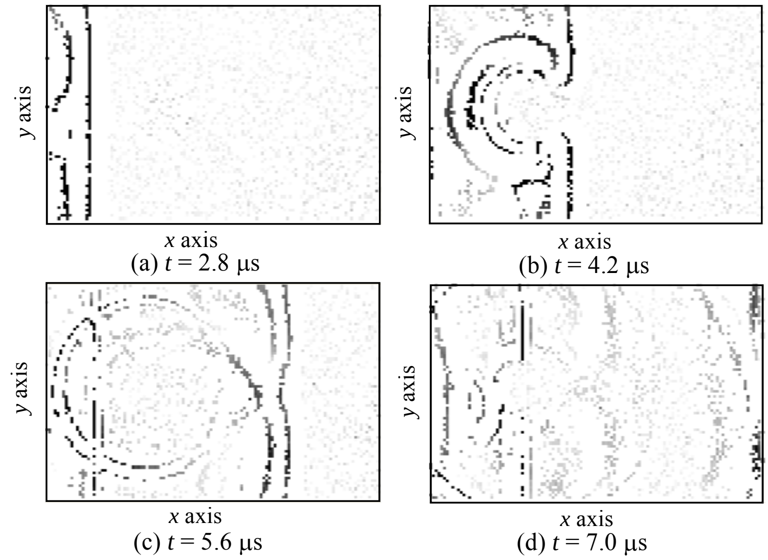

Fig. 5B Two-dimensional snapshots at (a) $t = 2.8$ μs, (b) $t = 4.2$ μs, (c) $t = 5.6$ μs, (d) $t = 7.0$ μs at the 0% threshold level

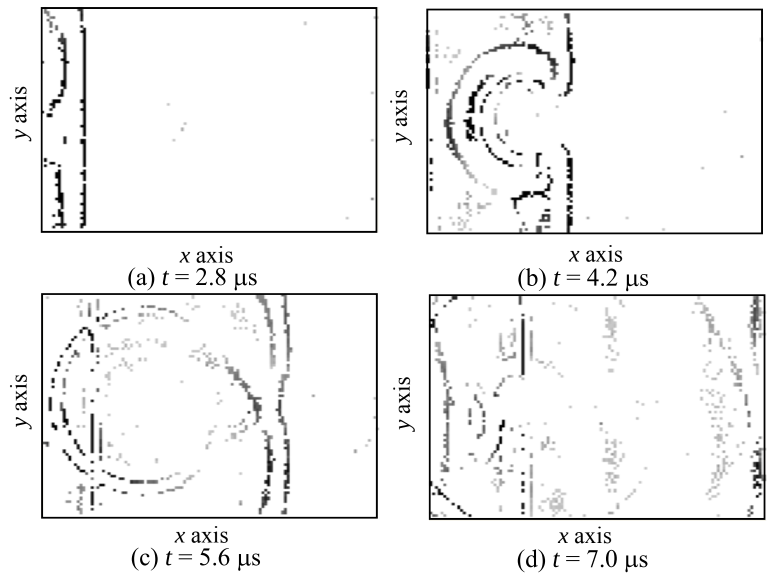

Fig. 5C Two-dimensional snapshots at (a) $t = 2.8$ μs, (b) $t = 4.2$ μs, (c) $t = 5.6$ μs, (d) $t = 7.0$ μs at the 5% threshold level

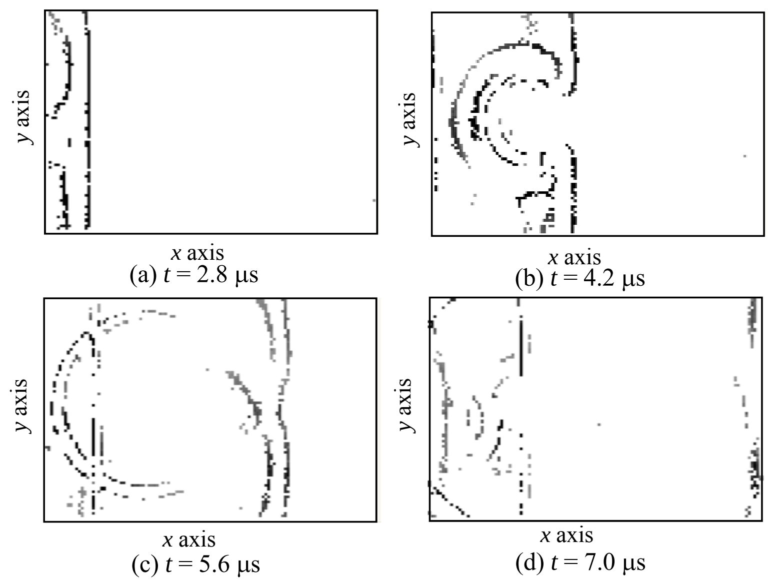

Fig. 5D Two-dimensional snapshots at (a) $t = 2.8$ μs, (b) $t = 4.2$ μs, (c) $t = 5.6$ μs, (d) $t = 7.0$ μs at the 10% threshold level

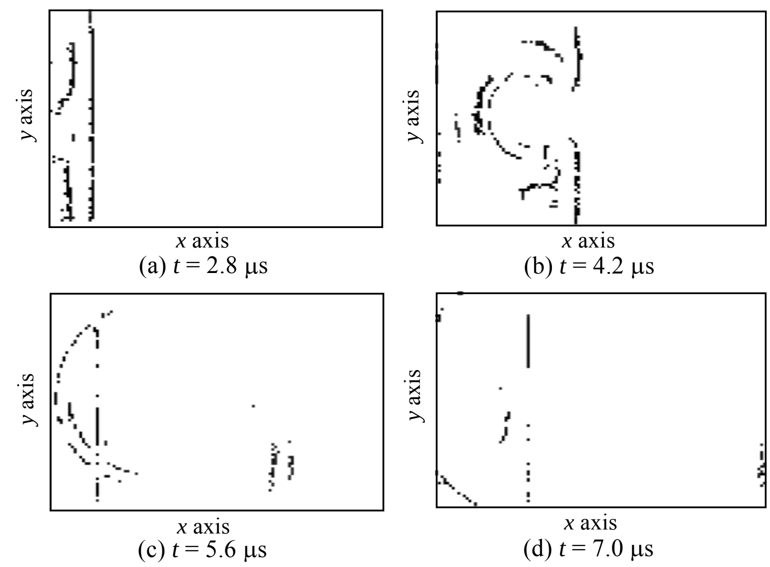

Fig. 5E Two-dimensional snapshots at (a) t = 2.8 μs, (b) t = 4.2 μs, (c) t = 5.6 μs, (d) t = 7.0 μs at the 20% threshold level

B. Determination of the Center Location of a Circle

Figure 6 shows the geometric relationships used to determine the center location of a circle from three points along its circumference. The center of the circle is found from the intersection point of two straight lines that orthogonally pass through the two midpoints for three points along the circumference of the circle. In Figure 6, the three points along the circumference of the circle are defined as $A_1(x_1, y_1)$, $A_2(x_2, y_2)$, and $A_3(x_3, y_3)$, which correspond to the preprocessed pixel points within the laser scanning area of the specimen. All combinations of three points extracted among all pixel points after preprocessing are selected. Two midpoints in the straight segments A_1A_2 and A_2A_3 are presented as $P(x_P, y_P)$ and $Q(x_Q, y_Q)$, respectively. The center point of the circle is then $C(x_C, y_C)$.

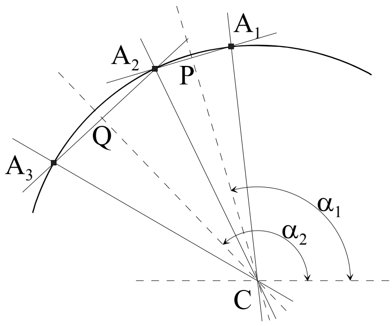

Fig. 6 Geometry used to derive the center position of a circle

In this case, two straight lines CP and CQ passing through the center point of the circle are expressed by using the gradient $\tan\alpha_1$ and $\tan\alpha_2$.

$$\begin{cases} y - y_c = \tan\alpha_1 (x - x_c) \\ y - y_c = \tan\alpha_2 (x - x_c) \end{cases} \tag{1}$$

where the angles α_1 and α_2 are expressed as:

$$\begin{cases} \alpha_1 = \arctan\left(\dfrac{y_2 - y_1}{x_2 - x_1}\right) + \dfrac{\pi}{2} \\ \alpha_2 = \arctan\left(\dfrac{y_3 - y_2}{x_3 - x_2}\right) + \dfrac{\pi}{2} \end{cases} \tag{2}$$

Substituting the two midpoints P and Q in Eq. (1) gives:

$$\begin{cases} y_P - y_C = \tan\alpha_1 (x_P - x_C) \\ y_Q - y_C = \tan\alpha_2 (x_Q - x_C) \end{cases} \tag{3}$$

By solving Eq. (3), the center point of the circle C is obtained as:

$$\begin{cases} x_C = \dfrac{y_P - y_Q - x_P \tan\alpha_1 + x_Q \tan\alpha_2}{\tan\alpha_2 - \tan\alpha_1} \\ y_C = y_P - (x_P - x_C)\tan\alpha_1 \end{cases} \tag{4}$$

The midpoints $P(x_P, y_P)$ and $Q(x_Q, y_Q)$ and the gradients $\tan\ \alpha_1$ and $\tan\alpha_2$ are straightforwardly obtained from the pixel points defined as $A_1(x_1, y_1)$, $A_2(x_2, y_2)$, and $A_3(x_3, y_3)$. Therefore, x_C is solved from Eq. (4). This step is applied to all combinations of the three points selected from all pixel points in the snapshot image after preprocessing the original measurement data. The contour map in the defect center location can be sketched by counting the number of intersection points of the two straight lines on the discrete grid (pixel) surface of the specimen. The estimation accuracy is determined by the grid width that is small enough to determine the defect location. Using this approach, the center location of the circle is estimated.

C. Defect Location Estimation

Figures 7A–D show the counter maps of the estimated center location of the hole at the 5%, 10%, 20%, and 30% threshold levels, respectively. At the 0% threshold, the defect location could not be determined even within a timeframe of several minutes, because of the large computational workload of a great number of peak points. In Figure 7A, four types of snapshots at *t* = 2.8 μs, 4.2 μs, 5.6 μs, and 7.0 μs are presented. In these figures, the maximum levels are normalized at each timestep to improve the visibility of the contour maps. In this calculation, all combinations of the three points extracted from all pixel peaks after preprocessing are considered. Therefore, when three points are on the line such as incident waves, there is no intersection point on the surface of the specimen, and in this case it is dismissed from consideration.

In Figure 7A, a small dark spot is observed in the vicinity of the center of the hole in the snapshot at *t* = 4.2 μs. The point (8.75 mm, 10.5 mm) in the scanned area in the specimen is detected as the defect center. The center point of the cylindrical hole is located at the point (10 mm, 10 mm) with the dia. 5.6 mm. Therefore, reasonable agreement between the two is observed. At *t* = 2.8 μs, because there is no scattering wavefront to determine the defect location (only the incident wave is observed) as shown in Figure 5C, the dark area indicating the defect center is widely distributed and the apparent defect center location cannot be observed. At *t* = 5.6 μs, the dark spots are distributed over a spread-out area. Figure 5C shows that the circular-shaped backscattering wavefront is important for defect detection together with the incident surface wave and the forward diffracted wave. However, compared to the snapshot of *t* = 4.2 μs, as time passes, the more that complex wavefronts, including multi-reflections, seem to affect the incomplete convergence. At *t* = 7.0 μs, the presence of circular-shaped wavefronts is no longer confirmed by Figure 5C. The dark spot is vague and the defect location is unclear. These results indicate that the timestep immediately after reflection from the hole is the suitable instant to accurately estimate the defect location.

The 5% and 10% threshold levels (Figs. 7A, B, respectively) show similar tendencies. In Figure 7B (10% threshold), the defect center location estimated in the snapshot of *t* = 4.2 μs is the point (8.75 mm, 10.5 mm) and is exactly the same as that in Figure 7A (5% threshold). In the 20% and 30% threshold levels (Figs. 7C, D, respectively), however, the defect center location does not converge even in the snapshot at *t* = 4.2 μs. In this case, the threshold level is very large and the number of extracted peaks is not enough to determine the defect location properly. In Figure 7D, this effect becomes particularly pronounced. These data show that threshold levels of 5%–10% are most desirable in determining the location of the defect center.

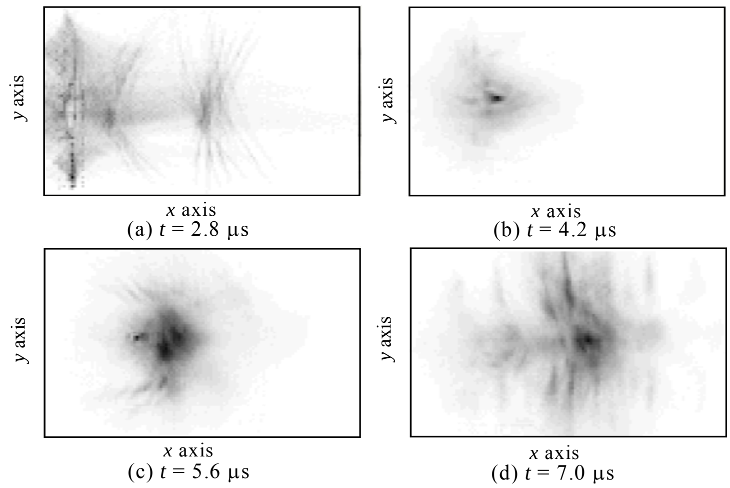

Fig. 7A Two-dimensional contour map for estimation of the defect location at (a) *t* = 2.8 μs, (b) *t* = 4.2 μs, (c) *t* = 5.6 μs, (d) *t* = 7.0 μs at the 5% threshold level

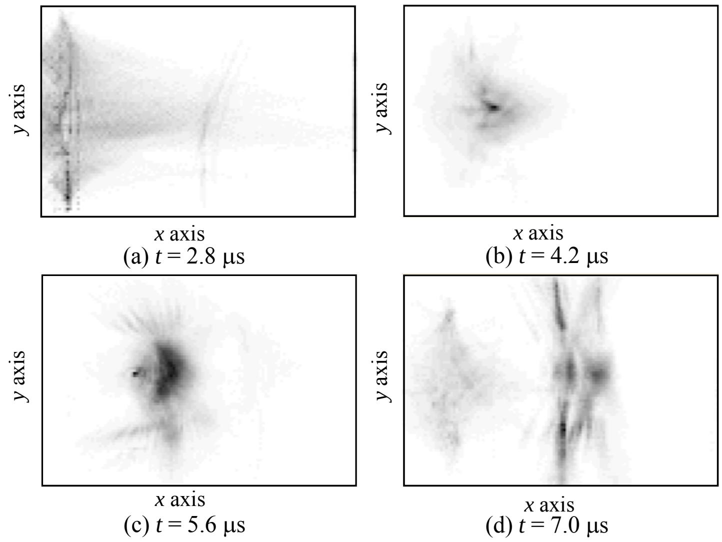

Fig. 7B Two-dimensional contour map for estimation of defect location at (a) t = 2.8 μs, (b) t = 4.2 μs, (c) t = 5.6 μs, (d) t = 7.0 μs at the 10% threshold level

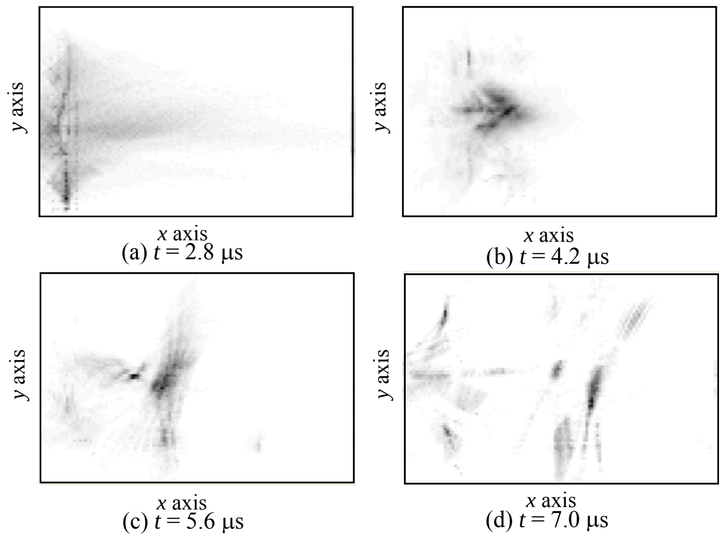

Fig. 7C Two-dimensional contour map for estimation of defect location at (a) t = 2.8 μs, (b) t = 4.2 μs, (c) t = 5.6 μs, (d) t = 7.0 μs at the 20% threshold level

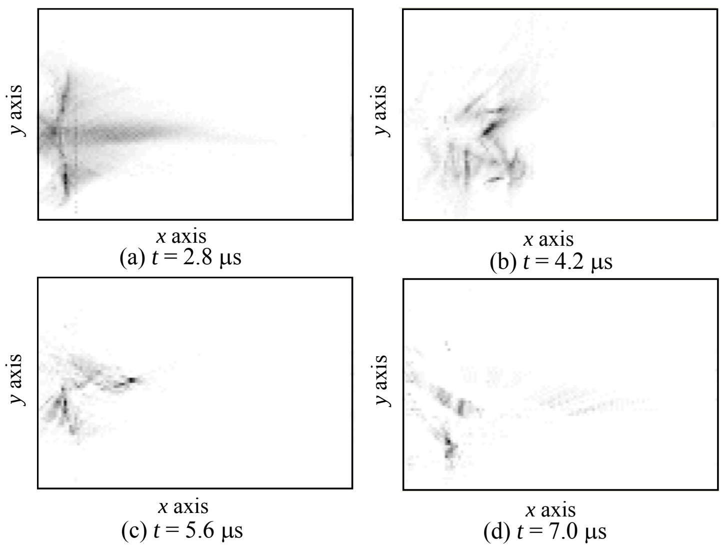

Fig. 7D Two-dimensional contour map for estimation of defect location at (a) t = 2.8 μs, (b) t = 4.2 μs, (c) t = 5.6 μs, (d) t = 7.0 μs at the 30% threshold level

D. CPU Time

Figure 8 shows the number of non-zero (peak) points as a function of the threshold level. These non-zero (peak) points are the preprocessed (peak-extracted and thresholded) points from the original measurement data to estimate the center location. The total number of original measurement points of n_{max} = 4809600 decreases very markedly around 800000 by applying peak extraction (0% threshold level). The number of non-zero points further decreases by applying a threshold level greater than 0%; the 5%, 10%, and 15% threshold levels correspond to non-zero points of ~400000, ~200000, and ~100000, respectively. The 5% threshold level halves the number of non-zero points in the 0% threshold level. Similarly, a threshold level of 10% and 15% halves the number of non-zero points in the threshold levels of 5% and 10%, respectively. These data indicate that by applying a threshold level greater than 5%, the percentage of non-zero points becomes less than 10% of the total number of original measurement points. This marked reduction in the number of peak points contributes to the enhancement of computational efficiency.

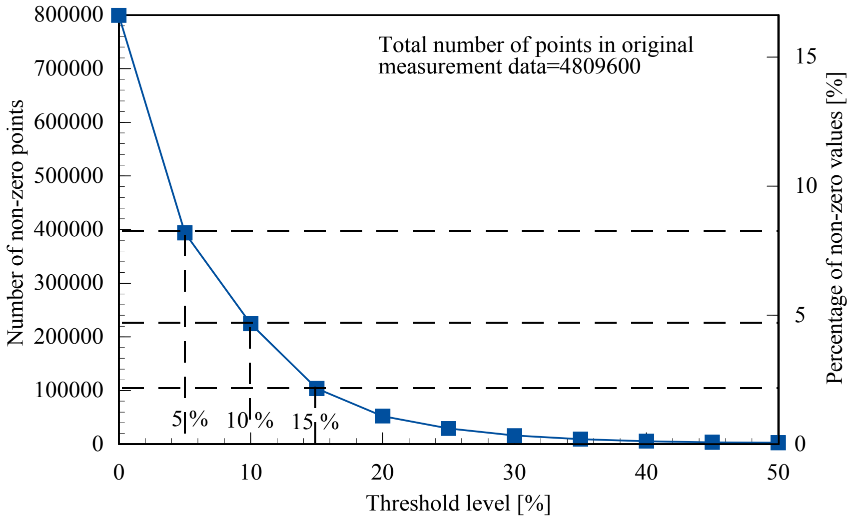

Fig. 8 Number of non-zero points as a function of the threshold level after the data preprocessing

Figure 9 shows the elapsed CPU time as a function of the threshold level. Seven types of snapshots at t = 2.8 μs, 4.2 μs, 5.6 μs, 7.0 μs, 8.4 μs, 9.8 μs, and 11.2 μs were calculated. The comparison of CPU time used is expressed from the viewpoint of the CPU workload of the source code. A desktop PC with a 3.16-GHz Intel Core2 Duo processor and 3 GB of RAM was used as the computational medium throughout this study. A GNU Fortran 95 (G95) was used as a compiler. The CPU time is obtained from the time difference of the built-in subroutine `CPU_Time` intercalated at the first and last parts in the main source code. As shown in Figure 9, at t = 4.2 μs, i.e., immediately after reflection from the hole, a defect detection CPU time less than 10 s is attained. As the threshold level is lower, more CPU time is required, because a great number of peaks including superfluous ones are incorporated into the calculation. As the time of the snapshots is increased, more CPU time is needed. This is because with the passing of time, the number of pixel points required for estimation increases as a result of multi-reflection at the defect and at the specimen periphery.

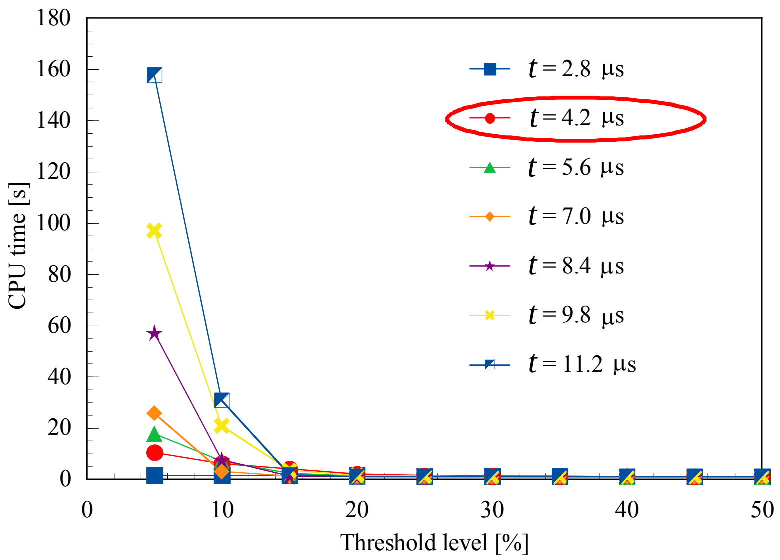

Fig. 9 CPU time as a function of the threshold level for various snapshots

III. CONCLUSION

We estimated a defect's location from the circular-shaped wavefront of the scattering waves. A pulsed laser scanning system was used to measure the data needed for defect location. An aluminum alloy plate with a drill hole at the center was the specimen. Data preprocessing consisted of two steps: peak extraction from the measured data and the suitable application of a threshold level to the extracted peaks. The defect location was accomplished using the scattering wavefront observed immediately after reflection from the defect. As a result of decreasing a great number of pixel points, efficient estimation can be obtained. The automation of defect detection for non-experts in a non-destructive way is highly desirable in a variety of industrial fields. A pulsed laser scanning technique such as this is not only powerful but can also be computerized as described. Future studies on the proposed system will focus on the effect of defect size, the detection of internal defects, and the detection of more complex-shaped flaws.

ACKNOWLEDGMENT

This research was partially supported by the Supporting Industry Project for Core Manufacturing Technology of Small and Medium Enterprise Agency (SME), Japan and a Grant-in-Aid for Scientific Research (C), (Grant No.25420426) of Japan Society for the Promotion of Science (JSPS), Japan.

REFERENCES

[1] J. Takatsubo, B. Wang, H. Tsuda, and N. Toyama, "Generation laser scanning method for the visualization of ultrasounds propagating on a 3-D object with an arbitrary shape," *Journal of Solid Mechanics and Materials Engineering*, vol. 1, iss. 12, pp. 1405-1411, 2007.

[2] S. Yashiro, J. Takatsubo, and N. Toyama, "An NDT technique for composite structures using visualized Lamb-wave propagation," *Composites Science and Technology*, vol. 67, pp. 3202-3208, 2007.

[3] J. Lee, J. Takatsubo, N. Toyama, and D. Kang, "Health monitoring of complex curved structures using an ultrasonic wavefield propagation imaging system," *Measurement Science and Technology*, vol. 18, pp. 3816-3824, 2007.

[4] S. Yashiro, J. Takatsubo, H. Miyauchi, and N. Toyama, "A novel technique for visualizing ultrasonic waves in general solid media by pulsed laser scan," *NDT&E International*, vol. 41, pp. 137-144, 2008.

[5] J. Takatsubo, H. Miyauchi, H. Tsuda, N. Toyama, K. Urabe, and B. Wang, "Generation laser scanning method for visualizing ultrasonic waves propagating on 3-D object," *1st International Symposium on Laser Ultrasonics: Science, Technology and Applications*, Jul. 2008.

[6] J. Takatsubo, B. Wang, H. Miyauchi, H. Tsuda, N. Toyama, and K. Urabe, "Laser ultrasonic technique for visualizing ultrasonic waves propagating on 3-D object," *17th World Conference on Nondestructive Testing (WCNDT2008)*, Oct. 2008.

[7] B. Wang, J. Takatsubo, N. Toyama, and M. Zhao, "The development of laser ultrasonic visualization equipment and its application in non-destructive inspection," *17th World Conference on Nondestructive Testing (WCNDT2008)*, Oct. 2008.

[8] S. Yashiro, N. Toyama, J. Takatsubo, and T. Shiraishi, "Laser-generation based imaging of ultrasonic wave propagation on welded steel plates and its application to defect detection," *Materials Transactions*, vol. 51, iss. 11, pp. 2069-2075, Nov. 2010.

[9] J. Takatsubo, M. Imade, Q. Fan, and S. Yamamoto, "Visualization of elastic waves by digital laser ultrasonics," *Transactions of the Japan Society of Mechanical Engineers*, Series C, vol. 65, iss. 639, pp. 4299-4304, Nov. 1999 (in Japanese).

[10] P. Viola, and M. Jones, "Rapid object detection using a boosted cascade of simple features, " *Proceedings of the 2001 IEEE Computer Society Conference on Computer Vision and Pattern Recognition*, vol. 1, pp. I-511-I-518, 2001.

[11] P. Viola, and M. Jones, "Robust Real-time Object Detection," *Second International Workshop on Statistical and Computational Theories of Vision-Modeling, Learning, Computing, and Sampling*, Jul. 2001.

[12] K. G. Hall, "Observing ultrasonic wave propagation by stroboscopic visualization methods," *Ultrasonics*, vol. 20, pp. 159-167, 1982.

[13] H. U. Li, and K. Negishi, "Visualization of lamb mode patterns in a glass plate," *Ultrasonics*, vol. 32, pp. 243-248, 1994.

[14] R. D. Huber, R. B. Mignogna, K. E. Simmonds, R. S. Schechter, and P. P. Delsanto, "Dynamic full-field visualization of ultrasound interacting with material defects: experiment and simulation," *Ultrasonics*, vol. 35, pp.7-16, 1997.

[15] J. A. Scales, and A. E. Malcolm, "Laser characterization of ultrasonic wave propagation in random media," *Physical Review E*, vol. 67, pp. 046618-1-7, 2003.

[16] T. E. Michaels, M. Ruzzene, and J. E. Michaels, "Frequency-wavenumber domain methods for analysis of incident and scattered guided wave fields," *Proc. of SPIE*, vol. 7295, pp. 729513-1-12, 2009.

[17] T. E. Michaels, J. E. Michaels, and M. Ruzzene, "Frequency-wavenumber domain analysis of guided wavefields," *Ultrasonics*, vol. 51, pp. 452-466, 2011.